Diffuse reflectance spectroscopy of the spine: improved breach detection with angulated fibers

Losch, M.S.; Kardux, Famke; Dankelman, J.; Hendriks, B.H.W.

DOI
10.1364/BOE.471725

Publication date
2023

Document Version
Final published version

Published in
Biomedical Optics Express

Citation (APA)
Losch, M. S., Kardux, F., Dankelman, J., & Hendriks, B. H. W. (2023). Diffuse reflectance spectroscopy of the spine: improved breach detection with angulated fibers. *Biomedical Optics Express*, *14*(2), 739-750. https://doi.org/10.1364/BOE.471725

Research Article | Vol. 14, No. 2 / 1 Feb 2023 / Biomedical Optics Express 739

Biomedical Optics EXPRESS

Diffuse reflectance spectroscopy of the spine: improved breach detection with angulated fibers

MERLE S. LOSCH,[1,*] FAMKE KARDUX,[1] JENNY DANKELMAN,[1] AND BENNO H. W. HENDRIKS[1,2]

[1]Department of Biomechanical Engineering, Delft University of Technology, Delft, The Netherlands
[2]Image Guided Therapy and Ultrasound Devices and System Department, Philips Research, Royal Philips NV, Eindhoven, The Netherlands
[*]m.s.losch@tudelft.nl

Abstract: Accuracy in spinal fusion varies greatly depending on the experience of the physician. Real-time tissue feedback with diffuse reflectance spectroscopy has been shown to provide cortical breach detection using a conventional probe with two parallel fibers. In this study, Monte Carlo simulations and optical phantom experiments were conducted to investigate how angulation of the emitting fiber affects the probed volume to allow for the detection of acute breaches. Difference in intensity magnitude between cancellous and cortical spectra increased with the fiber angle, suggesting that outward angulated fibers are beneficial in acute breach scenarios. Proximity to the cortical bone could be detected best with fibers angulated at $\theta_f = 45°$ for impending breaches between $\theta_p = 0°$ and $\theta_p = 45°$. An orthopedic surgical device comprising a third fiber perpendicular to the device axis could thus cover the full impending breach range from $\theta_p = 0°$ to $\theta_p = 90°$.

1. Introduction

Various diseases require patients to undergo spine surgery to correct for a deformity, to eliminate pain, or to treat an instability or fracture [1–3]. The prevailing treatment modality for these conditions is spinal fusion: a surgical procedure in which two or more vertebrae are "fused" together so that motion between them no longer occurs. The vertebrae are fixated in place using pedicle screws and connection rods. Pedicle screws are traditionally placed with the freehand technique, relying on anatomical landmarks for appropriate entry point selection [4,5]. The complex nature of the procedure coupled with the heavy reliance on anatomical knowledge results in high variability in accuracy rates of pedicle screw placement of between 27.6% and 100% reported in literature [6]. Commonly used image guidance systems include conventional fluoroscopy, two-dimensional and three-dimensional navigation [7]; however, Mason et al. [8] found up to 50.3% of screws were still misplaced when using conventional fluoroscopy, and up to 19.1% when using three-dimensional fluoroscopic navigation. As the spine is a very vulnerable anatomic region, exposing nearby neural and vascular structures to risk in the case of screw misplacement, real-time tissue feedback at the tip of the pedicle screw is required such that misplacement can be detected during insertion, allowing for on-the-fly trajectory adjustment by the surgeon.

Endoscopic ultrasound imaging allows for tissue characterization in the vertebra based on the acoustic properties of bone [9]. Low frequencies provide the most favorable conditions for cortical breach detection but offer very limited image resolution [10,11]. The variation of local tissue electrical impedance along the screw trajectory allows for the anticipation of cortical breaches through continuous conductivity measurements [12]. It does, however, not provide local signal direction.

Optical technologies enable directed measurements. Although Raman spectroscopy can be used to distinguish bone from other tissues based on their inelastic scattering behavior [13],

#471725 https://doi.org/10.1364/BOE.471725
Journal © 2023 Received 17 Aug 2022; revised 7 Dec 2022; accepted 14 Dec 2022; published 11 Jan 2023

Biomedical Optics EXPRESS

signal weakness leads to long acquisition times and makes it less suited for real-time surgical application. Photoacoustic imaging can be used during spine surgery to distinguish compact, high-amplitude signals originating from cortical bone from diffuse, low-amplitude cancellous bone signals [14,15]. Implementing photoacoustics into small surgical devices is still challenging, and the required components tend to be expensive [16].

In diffuse reflectance spectroscopy (DRS), light of different wavelengths is emitted into a biological tissue, in which it is either absorbed or scattered. The scattered light can be collected, resulting in a spectrum that maps the corresponding reflectance to every wavelength. From the magnitude and shape of the spectrum, characteristic absorption and scattering properties of the tissue can be derived [17–19]. These properties depend on the tissue composition and thus allow different tissues to be distinguished. DRS can be used to study the spectral characteristics of bone tissue in real time in a non-harmful way, and its relatively simple instrumentation allows for the integration into orthopedic surgical devices [20,21]. Previous studies have therefore proposed DRS measurements along the pedicle screw trajectory to assess fat content of the bone. The fat content varies along the transition zone of cancellous and cortical bone [22] and can be assessed to reliably anticipate cortical breaches [23–25].

These studies on DRS of the spine have used a conventional probe with two parallel fibers. However, studies on DRS for diagnostics of epithelial and dermatological conditions have shown promising results for manipulating the probed volume with the help of obliquely oriented fibers [26,27]. Wang et al. [26] have analyzed photon propagation through Monte Carlo (MC) simulations (λ = 500 nm) and found that detection shifts toward superficially scattered photons when the detector is angulated toward the emitting fiber. This fiber constellation, they conclude, could be used for stronger reflectance acquisition of the epithelial layer at a shallow depth, whereas angulating the collecting fibers away from the emitter primarily allows for the detection of photons scattered within the underlying stromal layer. Thilwind et al. [27] have investigated depth selectivity with obliquely oriented emitting fibers through two-layered optical phantom experiments and MC simulations in the NIR range. They found that angulating the emitting fiber toward the detector allows for selective probing of the epidermis by reducing contributions from the underlying layer of the dermis, whereas outward angulation allows for more selective probing of deeper layers.

In this study, we investigate how fiber angulation can further improve cortical breach detection to enhance spine surgery. We assume that fiber angulation does not only influence the probing depth, but will affect the probed volume entirely. As breaches typically impend at non-perpendicular angles due to anatomical conditions and entry point recommendations [28], fiber angulation may specifically help to anticipate cortical breaches impending at acute angles. We conduct MC simulations and compare them with absorption experiments to evaluate the effect of fiber angulation on the probed volume. We then conduct optical phantom experiments to evaluate the capability of breach detection with DRS for different fiber angulations in a variety of breach scenarios. While perpendicular breach detection is possible regardless of the fiber angulation, higher fiber angles allow for earlier detection of acute breaches.

2. DRS setup

A conventional probe for DRS contains two parallel optical fibers placed at a fiber distance d_f. Angulating one of these fibers will change the collected DRS signal. With the orientation of the collecting fiber fixed along the axis of the optical probe, we define the fiber angulation θ_f as the angulation of the emitting fiber away from the collecting fiber, in the plane of the two fibers.

Our DRS setup comprises a custom-designed optical probe (Fig. 1(a)-(b), CAD files available at Ref. [50]), equipped with two fibers (step-index multimode fiber optic patch cables, core diameter 200 μm, numerical aperture (NA) = 0.22, low OH, Thorlabs Inc., Newton (NJ), USA) at a fiber distance d_f = 1.4 mm to emit and collect light to and from the tissue. Due to constructive

Biomedical Optics EXPRESS

constraints, the collecting fiber cannot be placed in the frontal plane of the emiting fiber, but is in fact placed slightly behind the emitting fiber (lateral distance d_{fl} = 1 mm, transverse distance d_{ft} = 1 mm), see Fig. 1(c). The light emitting fiber can be angulated in the frontal plane to angles θ_f [°] ∈ {0, 15, 30, 45} and is connected to a tungsten halogen broadband light source with an integrated shutter (HAL-S, Avantes, Apeldoorn, The Netherlands). The light collecting fiber is oriented along the axis of the optical probe and is connected to a NIR spectrometer with an InGaAs detector (S330-2 NIR, HORIBA Scientific, Piscataway (NJ), USA) to collect light at 255 distinct wavelengths between 839.65 nm and 1724.27 nm. The DRS setup is shown in Fig. 1(d). The system is controlled using Philips custom-developed software.

Before the DRS measurements, the system was calibrated using a Spectralon white reference standard (WS-1-SL, Labsphere Inc., North Sutton (NH), USA). Both fibers were oriented along the axis of the optical probe, which was placed perpendicular to the standard at a distance of 3.2 mm, and an intensity calibration spectrum was acquired to compensate for any wavelength-dependent sensitivities in the setup.

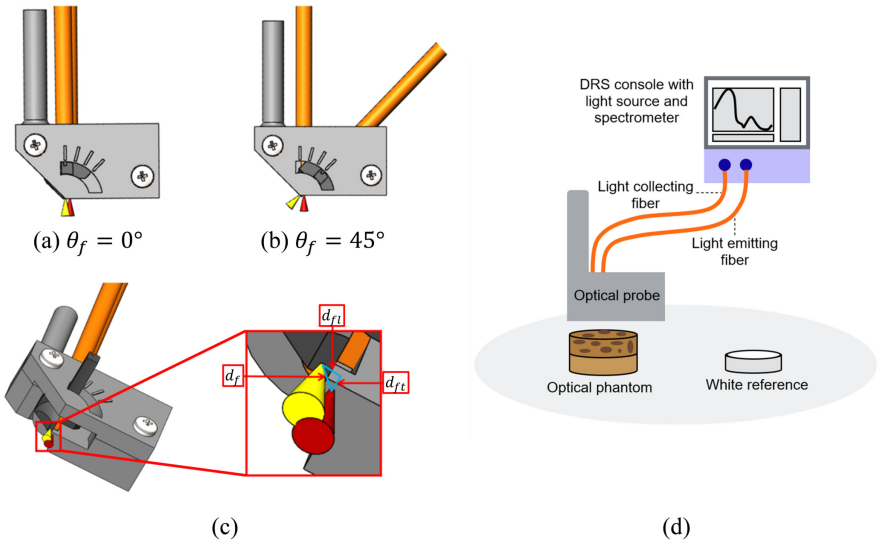

Fig. 1. (a)-(b) Illustration of the custom-designed optical probe. (c) Detailed view of the fiber constellation. (d) Illustration of the DRS setup. Direction and location of the emitting fiber are indicated with a yellow cone, direction and location of the light collecting fiber are indicated with a red cone.

3. Methods

3.1. Effect of fiber angulation on the probed volume

Monte Carlo simulations MC simulations were run to provide insight into the variation in probed volume for different fiber angulations. The simulations were carried out in MCmatlab [29], a radiative transfer equation (RTE) solver based on the mcxyz model developed by Jacques and Li [30] that conveniently combines the computational speed of C with the versatility of MATLAB. 10^9 photons of a wavelength of 1211 nm, corresponding to the most prominent absorption peak of fat in the NIR range [31], were emitted into a single-layer cancellous bone model (μ_a(1211 nm) = 1.4220, μ_s'(1211 nm) = 19.5129, g = 0.9 [24]) to investigate possible photon paths taken within this layer. The model dimensions were 4.0 mm x 4.0 mm x 3.0 mm with a resolution of 100 bins/mm (simulation run for 400 x 400 x 300 voxels).

Biomedical Optics EXPRESS

The setup of the simulation is illustrated in Fig. 2(a). The light source emitted light at a fiber angulation θ_f [°] $\in \{0, 15, 30, 45\}$. To model the DRS setup as closely as possible, the emitted light was approximated by a top-hat beam with a focal plane intensity distribution width of $1/2e^2$ times the optical fiber core diameter (200 μm) and an angular intensity distribution half-angle of $1/e^2$ times the inverse sine of the optical fiber NA (0.22). The light collector was defined as an optical fiber (core diameter 200 μm, NA = 0.22) at a fiber distance d_f = 1.4 mm.

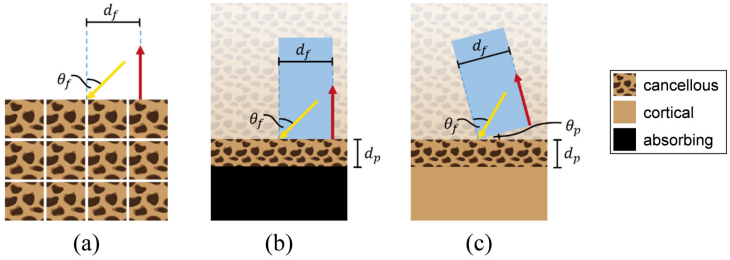

Fig. 2. Illustration of the fiber angulation setup for (a) the simulation (b) the absorption experiment (c) the optical phantom experiment. The simulation was run for 400 x 400 x 300 voxels. The pose of the optical probe is indicated in blue for the experimental setups. Direction and location of the emitting fiber are indicated with a yellow arrow, direction and location of the light collecting fiber are indicated with a red arrow.

Absorption experiments The results of the MC simulations were experimentally validated in an absorption experiment on a two-layered model consisting of a fully absorbing bottom layer and a cancellous bone-mimicking top layer. The fully absorbing layer consisted of matt black tape (HPX GB4850, Option Tape Specialties NV, Temse, Belgium). The cancellous bone-mimicking layer consisted of pure coconut milk with a fat content of 18% (Go-Tan B.V., Kesteren, The Netherlands), which is a cheap and simple alternative to the Intralipid 20% IV fat emulsion (Baxter International Inc., Deerfield (IL), USA) commonly used for tissue-mimicking phantoms [32–34]. Inhomogeneity in lipid droplet size – which will be less controlled for an aliment like coconut milk than for Intralipid, an approved intravenous nutritional product – will affect the scattering properties; the absorption properties, however, are most likely not affected [31]. Absorption in the NIR range is also comparable among animal fat and plant-based fat as shown by the same study (for beef lipid vs. 100% lipid sunflower oil).

The setup of the absorption experiment is illustrated in Fig. 2(b). The probe was mounted onto a manual 25 mm linear translation stage (Thorlabs Inc., Newton (NJ), USA). At various distances to the absorbing layer d_p [mm] $\in \{0, 0.2, \ldots, 3\}$, diffuse reflectance was measured with the DRS setup described above, varying the fiber angulation θ_f [°] $\in \{0, 15, 30, 45\}$. The probe was oriented perpendicular to the interface of the two model layers. Light intensity was measured at λ = 1211 nm; ten intensities were obtained at every distance. Integration time was set to 1000 ms.

3.2. *Effect of fiber angulation on the capability of breach detection*

To enhance spine surgery with a DRS probe with modified fiber angulation, it should allow to anticipate cortical breaches in a variety of different scenarios. A breach scenario is defined by two parameters θ_p and d_p that describe the pose of the optical probe relative to the tissue interface, which we assume to be locally plane. The probe angulation θ_p describes the angulation of the probe relative to the tissue interface. As this study aims at investigating how a modified fiber angulation can help to anticipate acute breaches, the probe is always angulated in favor of the modified probe (i.e. in opposite direction of the fiber angulation), in the fiber plane. The distance

Biomedical Optics EXPRESS

to breach d_p describes the shortest distance between the distal end of the emitting fiber and the tissue interface.

Optical phantom experiments To study the effect of fiber angulation on the measured diffuse reflectance spectrum and its influence on detecting proximity to the cortical bone boundary, an experiment was conducted on a two-layered optical phantom consisting of a cortical bone-mimicking bottom layer and a cancellous bone-mimicking top layer. The cortical bone-mimicking layer was made of water and gelatin following the production process described by Azizian Amiri et al. [35] (without addition of a lipid component). Demineralized water was mixed with NaCl (ALDI Inkoop B.V., Culemborg, The Netherlands), to which barium sulfate (Acros Organics B.V.B.A., Geel, Belgium) was added as a scattering agent. 15% gelatin (250 bloom porcine gelatin powder, Dr. Oetker, Bielefeld, Germany) was added as emulsifier and gelling agent, and sodium benzoate (Natural Spices B.V., Mijdrecht, The Netherlands) was added as a preservative. The quantities for 100 ml of phantom are listed in Table 1. As for the absorption experiment, the cancellous bone-mimicking layer consisted of pure coconut milk with a fat content of 18%.

Table 1. Composition of the cortical bone-mimicking layer

water (ml)	NaCl (g)	barium sulfate (g)	gelatin (g)	sodium benzoate (g)
100	1	3	15	0.1

The setup of the optical phantom experiment is illustrated in Fig. 2(c). The probe was mounted onto a manual 25 mm linear translation stage (Thorlabs Inc., Newton (NJ), USA). At various distances to the interface of the two phantom layers d_p [mm] $\in \{0, 0.25, \ldots, 2.5\}$, diffuse reflectance spectra were obtained with the DRS setup described above, varying the fiber angulation θ_f [°] $\in \{0, 15, 30, 45\}$. The probe was angulated by θ_p [°] $\in \{0, 15, 30, 45\}$. Ten spectra were registered and averaged at every location. Integration time was set to 1000 ms. The experiment was repeated three times at different points within the phantom. The averaged spectra were filtered with a third-order Savitzky-Golay filter with a frame length of 11 to remove noise. The effect of the fiber angulation on the measured diffuse reflectance spectrum was determined for a wavelength range from 1000 nm to 1400 nm. All spectra were normalized to $\lambda_0 = 1211$ nm. Additionally, from these normalized spectra, the change in maximal intensity when approaching the interface was retained to allow for the quantitative comparison of the performance between different fiber angulations in a breach scenario. The total increase in intensity at the interface ($d_f = 0$ mm) was statistically evaluated in an analysis of variance (ANOVA) with post-hoc Tukey's honest significant difference (HSD) test at a significance level of 5%.

4. Results

4.1. Effect of fiber angulation on the probed volume

To provide insight into the probed volume for angulated fibers, Fig. 3(a) shows the normalized fluence rate of collected photons for $\theta_f = 0°$ orthogonally projected onto the plane of the two fibers. The normalized fluence rate is a three-dimensional matrix of the accumulated energy deposited into the voxels as photon packets propagate through the simulation volume, normalized to the input power and divided by the absorption coefficient to yield the irradiance of every voxel [29]. The normalized fluence rate is overlaid with the approximated probed volume (comprising the paths followed by 68.3% (mean ± 1 std) of all detected photons) for all simulated fiber angulations (θ_f [°] $\in \{0, 15, 30, 45\}$). The plot shows that the probed volume can be manipulated with the help of obliquely oriented fibers. The effect is predominant in the superficial tissue close to the emitting fiber, where the emitted light is deflected outward and propagates through a wider tissue volume for higher angulations. Along the photon path, the difference in probed volume

Biomedical Optics EXPRESS

among the fiber angles decreases. Close to the collecting fiber, the probed volume is completely unaffected by the fiber angulation. The probing depth is similar for all fiber angulations.

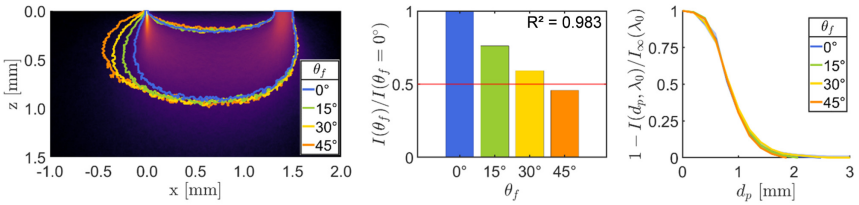

(a) (b) (c)

Fig. 3. (a) Projected normalized fluence rate of collected photons for $\theta_f = 0°$ with indication of approximated probed volume (comprising the paths followed by 68.3% of all detected photons) for different fiber angles. (b) Photon count for different fiber angles relative to the photon count observed for $\theta_f = 0°$. Red line indicates half of the original photon count. (c) Absorption ratio per distance to the absorbing layer for different fiber angles.

The MC simulations show that the total photon count decreases linearly with the angulation ($R^2 = 0.983$), as shown in Fig. 3(b). For $\theta_f = 45°$, the photon count has decreased to less than half of the photon count observed for $\theta_f = 0°$.

Figure 3(c) shows the ratio of absorbed photons per distance to the absorbing layer (calculated based on the photon count at the respective distance relative to the photon count observed for $d_p \to \infty$) for different fiber angles. The mean absorption ratio for $\theta_f = 0°$ is displayed as a solid line together with the 95% confidence interval highlighted in the same color. The mean absorption ratios for the other fiber angulations were plotted as solid lines in the same plot to illustrate how the fiber angulation influences probing depth and sensitivity of DRS to certain tissue depths. Despite the observation that the probed volume changes with θ_f, the absorption experiment shows that the curves for the mean absorption ratios for fiber angles $\theta_f > 0°$ lie within the confidence interval of the mean absorption ratio for $\theta_f = 0°$.

4.2. *Effect of fiber angulation on the capability of breach detection*

To illustrate the influence of obliquely oriented fibers on the detection of proximity to the cortical bone boundary, Fig. 4 and 5 show typical plots of the normalized reflectance spectra for approaching the interface at the two most extreme angles $\theta_p = 0°$ and $\theta_p = 45°$, respectively, for different fiber angulations θ_f. All spectra are plotted relative to the normalized reflectance spectrum acquired on the pure cancellous bone-mimicking phantom ($d_p \to \infty$) for the respective fiber angulation. In this way, we reconstruct a pedicle screw placement scenario in which a reference spectrum is acquired on cancellous bone at the start of the procedure. Continuous measurements along the screw trajectory allow to detect deviation from this reference spectrum, which indicates a change in tissue properties and warns the surgeon of an impending cortical breach.

A gradual change in spectrum is observed for approaching the cortical layer (blue to yellow) for all angles θ_p and θ_f. For $\theta_p = 0°$ (Fig. 4), the difference in intensity between cancellous and cortical bone-mimicking phantom is of similar magnitude for all fiber angles θ_f.

For $\theta_p = 45°$ (Fig. 5), the cortical curve for $\theta_f = 0°$ is visibly flatter than for approaching the interface perpendicularly, and the spacing between the spectral lines of individual distances is decreased. The spectral curves for the other fiber angulations are increasingly steeper, with the intensity difference for $\theta_f = 45°$ being the steepest and experiencing only minor change compared to $\theta_p = 0°$.

From the plots of all probe angulations ($\theta_p = 15°$ and $\theta_p = 30°$ not shown), it can be observed that the spectral curves for low fiber angulations flatten when the probe is angulated with regard to

Biomedical Optics EXPRESS

the interface. Higher fiber angulations produce steep spectra with intensity differences remaining at a similar magnitude even when the probe is angulated.

The performance of different fiber angulations in a breach scenario can be quantitatively compared with the help of the change in maximal intensity when approaching the interface, as illustrated in Fig. 6. The mean normalized change observed in the three experiments is displayed as a solid line together with the standard deviation highlighted in the same color. The steepness of the curve as well as the total increase in intensity provide information about how well a fiber angulation performs in a breach scenario. Asterisks indicate that the total increase in intensity at the interface is significantly different for two fiber angulations.

As indicated by the spectral curves in Fig. 4 and 5, the curves in Fig. 6 show a consistently increasing maximal intensity for approaching the interface. This is the case for all fiber angles and breach scenarios, with the exception of $\theta_f = 0°$ where the increase in maximal intensity is followed by a decrease at short distances to the interface ($d_p \leq 0.25$ mm) in the acute breach scenarios.

For $\theta_p = 0°$, no significant differences in total increase of maximal intensity at the interface were found in the ANOVA. For $\theta_p = 15°$, Tukey's HSD revealed that all fiber angulations yield total increases that are significantly different from that of $\theta_f = 0°$. For $\theta_p = 30°$, all fiber angulations yield total increases that are significantly different from that of $\theta_f = 0°$. Additionally, the increase for $\theta_f = 45°$ is significantly different from those for all other fiber angulations. For $\theta_p = 45°$, the total increases for $\theta_f = 30°$ and $\theta_f = 45°$ are significantly different from that of $\theta_f = 0°$.

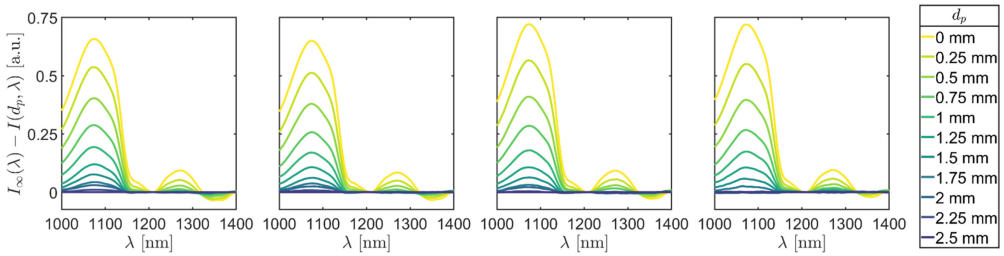

(a) $\theta_f = 0°$ (b) $\theta_f = 15°$ (c) $\theta_f = 30°$ (d) $\theta_f = 45°$

Fig. 4. Normalized reflectance spectra ($\lambda_0 = 1211$ nm) for different distances to the interface relative to the normalized reflectance spectrum of the pure cancellous bone-mimicking phantom, $\theta_p = 0°$.

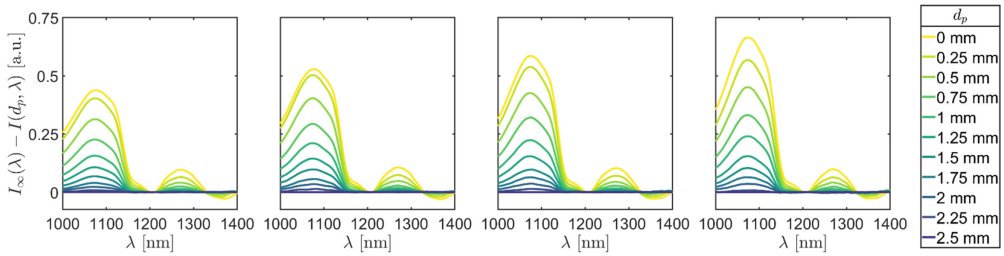

(a) $\theta_f = 0°$ (b) $\theta_f = 15°$ (c) $\theta_f = 30°$ (d) $\theta_f = 45°$

Fig. 5. Normalized reflectance spectra ($\lambda_0 = 1211$ nm) for different distances to the interface relative to the normalized reflectance spectrum of the pure cancellous bone-mimicking phantom, $\theta_p = 45°$.

Biomedical Optics EXPRESS

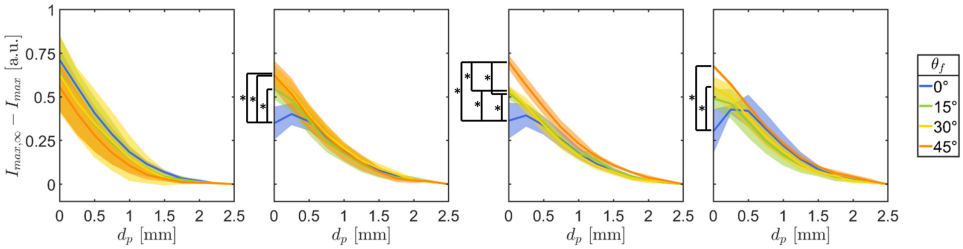

(a) $\theta_p = 0°$ (b) $\theta_p = 15°$ (c) $\theta_p = 30°$ (d) $\theta_p = 45°$

Fig. 6. Normalized change in maximal intensity (λ_0 = 1211 nm) for different fiber angles.

5. Discussion

The results from the MC simulations show that the probed volume around the emitting fiber can be manipulated with the help of angulated fibers. The high anisotropy factor g of biological tissues [36] accounts for the fact that, in a single scattering event, photons are typically scattered in the forward direction as described by the Henyey-Greenstein scattering function [37]. The propagation direction of photons close to the emitter hence heavily depends on the fiber angulation. At higher tissue depths, however, and after a high number of scattering events, total light diffusion occurs, and photons travel regardless of their initial propagation direction [38]. Angulation therefore has only limited potential to change the probed volume, and the probing depth remains unchanged by the fiber angulation.

These observations are confirmed by the absorption experiment that indicates that photons emitted at higher angles θ_f may follow a different path, but this deflection generally occurs within tissue of the same depth, as the ratio of photons absorbed at every distance to the absorbing layer is not influenced by θ_f. Angulating the emitting fiber away from the collector hence does not influence the probing depth or sensitivity of DRS to certain tissue depths.

The influence of fiber angulation on the probing depth has previously been investigated in the context of epithelial precancer detection [26] and for the diagnosis of precancerous skin lesions [27]. In both studies, the aim of the researchers was to decrease the detection depth of DRS with the help of a short fiber distance and oblique fibers in order to probe superficial layers without the contribution of underlying tissue layers. The selected fiber distances, in combination with fibers angulated toward each other, lead to a low number of scattering events [27] and indeed allow for selective probing of surface tissue layers. In contrast, we in our study aim at manipulating the probed volume in order to sense sideways and allow for the earlier detection of non-perpendicular breaches, which is why we selected a larger fiber distance for higher detection depth. With our setup, we emit photons away from the detector, so photons propagate outward and travel further before their detection. After a high number of scattering events, light is totally diffuse, and the probing depth is not influenced by the fiber angle.

The MC simulations further show that the total photon count decreases for oblique fibers, leading to a lower signal-to-noise ratio (SNR) for higher fiber angles. For $\theta_f = 45°$, the photon count, and thus also the SNR, has decreased by half compared to the photon count for two parallel fibers. This is because of the angular dependence of light scattering. In bone tissue, mineralized structures cause tissue anisotropy [39], leading to a tendency toward forward scattering that causes more photons to travel away from the detector when emitted at higher angles. A second reason is that the length of the average path taken by a photon before reaching the detector increases when the photon is emitted at a higher angle. On this longer path, more absorption events take place according to Beer-Lambert law [40], leading to a lower photon count at the detector. The decrease in total reflectance is in line with findings from previous studies [26].

Biomedical Optics EXPRESS

This decreased SNR does not seem to have a negative influence on the capability of breach detection, as shown by the results of the optical phantom experiments. Difference in intensity between cancellous and cortical bone-mimicking phantom could be observed for all probe and fiber angulations.

For $\theta_p = 0°$, the difference in intensity between cancellous and cortical bone-mimicking phantom is independent from the fiber angulation θ_f. This is in line with the findings from the MC simulations and absorption experiments that the probing depth and sensitivity of DRS to certain tissue depths are unaffected by angulating the emitting fiber away from the collector. It indicates that perpendicular breach detection is possible regardless of the fiber angulation.

For $\theta_p > 0°$, the difference in intensity between cancellous and cortical bone-mimicking phantom increases with the fiber angulation θ_f. Hence, the influence of approaching the cortical layer becomes more evident in the spectra for higher fiber angles. This increase in spectral change indicates earlier detection of proximity to the cortical bone boundary with angulated fibers for breaches impending at acute angles.

This is supported by the change in maximal intensity observed for different fiber angulations. The curves show that all fiber angulations succeed to detect breaches thanks to an increase in intensity when approaching the cortical layer. Performance of all fiber angles is similar in a perpendicular breach scenario, whereas higher fiber angles perform better for acute breaches, as shown in the ANOVA.

For acute breach angles, the spectra observed for $\theta_f = 0°$ experience a decrease at short distances to the interface. This reflectance change at the interface is most likely due to a refractive index mismatch, causing specular reflection at the interface of the two phantom layers. At higher fiber angulations, this effect is not produced due to the constellation of emitting and collecting fiber that decreases the susceptibility to detect specular reflection [41]. This decrease also explains the significant difference observed in the ANOVA. Only for $\theta_p = 30°$, the highest fiber angle ($\theta_f = 45°$) performs significantly better than all other fiber angulations.

Overall, our results show that breaches of all tested scenarios can be detected with any fiber constellation, although higher fiber angles tend to perform better in acute breach scenarios. This indicates that manufacturers should aim to produce probes with high fiber angles (e.g. $\theta_f = 45°$) capable of detecting breaches at both $\theta_p = 0°$ and $\theta_p = 45°$. Small deviations of angle during the production process will however not restrain the probe's ability to detect breaches.

Limitations In our MC simulations, emitter and collector are placed in the same frontal plane ($y = 0$ mm). In our DRS setup, however, the collecting fiber needed to be placed at a (short) transverse distance to the emitter due to constructive constraints. As the total fiber distance was identical for simulations and experiments ($d_f = 1.4$ mm), we neglect the influence of the transverse distance and assume that the angulation occurs in the plane of the two fibers both times.

Another simplification in our experiments is the use of coconut milk for the cancellous bone-mimicking phantom. This choice is justified by the findings of Nachabé et al. [31].

Generally, phantoms can represent the optical tissue properties of vertebrae only to a limited extent, especially since the fat content of the cancellous bone-mimicking phantom was only 18%, which is much lower than the actual fat content of cancellous bone in vertebrae [22,42]. However, this makes our study results applicable to many more medical scenarios in which DRS is used to distinguish tissues based on their fat content, such as for instance tumor detection and margin assessment in oncology [43–45] and needle guidance in anesthesia [46,47]. In actual vertebrae, we would expect the difference in spectrum to be even more pronounced due to the elevated fat content of the cancellous bone.

It is an arbitrary choice to angulate the emitting fiber, but due to the time reversal invariance of Maxwell's equations, we assume the reverse process to be almost the same as the forward process. Thus, angulating either of the fibers will yield the same spectral curves. Yet, in an orthopedic

Biomedical Optics EXPRESS

surgical device, alternatives to implement light beam steering need to be found, as fiber bending is limited to the minimum bending radius of the selected optical fiber and constrained by the dimensions of the device (typically in the range of a few millimeters). Possible solutions for emitting or collecting light at an angle off-axis are reflection/refraction or diffraction of light within the probe [48]. Light beam steering with the help of optical elements such as mirrors, however, will cause divergence within the probe. This can influence the probed volume observed in our MC simulations as well as the spectra observed in our experiments, and moreover leads to further reduction of the SNR. Converging optical elements can solve the loss of photons and increase the SNR. The space around the optical elements should be filled up with fully transparent material with a refractive index matched to blood to prevent light reflection and refraction at the interface between probe and tissue.

Although both, reflectance spectra and quantitative comparison, show a clear trend for the difference in intensity when approaching the cortical layer at acute angles with different fiber angulations, the ANOVA only reveals significance for comparing curves of $\theta_f = 0°$ and higher fiber angles, mainly thanks to the decreased intensity at the interface for two parallel fibers. The low significance of the curve comparisons among higher fiber angles can be attributed to the limited number of experiments conducted ($n = 3$). More experiments would be needed to establish if there are indeed significant differences in performance between fiber angles.

Finally, more elaborate data interpretation with the help of spectral fitting [31] or a classification algorithm [25,49] is needed before DRS can actually be used during surgery.

6. Conclusion

DRS can enhance spine surgery by allowing to detect impending cortical breaches. This study investigated how fiber angulation can help to anticipate specifically non-perpendicular cortical breaches. With our results from MC simulations, absorption experiments and optical phantom experiments, we show how the use of obliquely oriented fibers allows to manipulate the probed volume to detect proximity to the cortical layer at acute angles. The increased difference in intensity for higher fiber angles suggests that cortical breach detection benefits from fiber angulation.

An orthopedic surgical device comprising two optical fibers to emit light off-axis ($\theta_f = 45°$) and collect light along the device axis can be used to detect proximity to the cortical bone boundary along the pedicle screw trajectory for impending breaches between $\theta_p = 0°$ and $\theta_p = 45°$. Adding a third fiber to collect light perpendicular to the device axis (at $\theta_f = 45°$ to the off-axis emitter) allows to cover the full impending breach range from $\theta_p = 0°$ to $\theta_p = 90°$.

Funding. Nederlandse Organisatie voor Wetenschappelijk Onderzoek (NWO-TTW 17553).

Disclosures. BHWH: Philips Research (E).

Data availability. Data underlying the results presented in this paper are available in Ref. [50].

References

1. S. L. Weinstein, L. A. Dolan, J. C. Cheng, A. Danielsson, and J. A. Morcuende, "Adolescent idiopathic scoliosis," Lancet **371**(9623), 1527–1537 (2008).
2. R. A. Deyo, D. T. Gray, W. Kreuter, S. Mirza, and B. I. Martin, "United states trends in lumbar fusion surgery for degenerative conditions," Spine **30**(12), 1441–1445 (2005).
3. W. Dick, P. Kluger, F. Magerl, O. Woersdörfer, and G. Zäch, "A new device for internal fixation of thoracolumbar and lumbar spine fractures: the 'fixateur interne'," Spinal Cord **23**(4), 225–232 (1985).
4. H. Boucher, "A method of spinal fusion," J. Bone Jt. Surg., Br. Vol. **41-B**(2), 248–259 (1959).
5. Y. J. Kim, L. G. Lenke, K. H. Bridwell, Y. S. Cho, and K. D. Riew, "Free hand pedicle screw placement in the thoracic spine: is it safe?" Spine **29**(3), 333–342 (2004).
6. V. Kosmopoulos and C. Schizas, "Pedicle screw placement accuracy: a meta-analysis," Spine **32**(3), E111–E120 (2007).
7. A. C. Bourgeois, A. R. Faulkner, A. S. Pasciak, and Y. C. Bradley, "The evolution of image-guided lumbosacral spine surgery," Ann. Transl. Med. **3**(5), 69 (2015).

Biomedical Optics EXPRESS

8. A. Mason, R. Paulsen, J. M. Babuska, S. Rajpal, S. Burneikiene, E. L. Nelson, and A. T. Villavicencio, "The accuracy of pedicle screw placement using intraoperative image guidance systems: a systematic review," J. Neurosurg. **20**(2), 196–203 (2014).
9. M. Mujagic, H. J. Ginsberg, and R. S. Cobbold, "Development of a method for ultrasound-guided placement of pedicle screws," IEEE Trans. Sonics Ultrason. **55**(6), 1267–1276 (2008).
10. E. Bossy, P. Laugier, F. Peyrin, and F. Padilla, "Attenuation in trabecular bone: A comparison between numerical simulation and experimental results in human femur," J. Acoust. Soc. Am. **122**(4), 2469–2475 (2007).
11. A.-H. Aly, H. J. Ginsberg, and R. S. Cobbold, "On ultrasound imaging for guided screw insertion in spinal fusion surgery," Ultrasound Med. Biol. **37**(4), 651–664 (2011).
12. C. Bolger, M. O. Kelleher, L. McEvoy, M. Brayda-Bruno, A. Kaelin, J.-Y. Lazennec, J.-C. Le Huec, C. Logroscino, P. Mata, P. Moreta, G. Saillant, and R. Zeller, "Electrical conductivity measurement: a new technique to detect iatrogenic initial pedicle perforation," Eur. Spine J. **16**(11), 1919–1924 (2007).
13. L. M. Fullwood, I. E. I. Petterson, A. P. Dudgeon, G. R. Lloyd, C. Kendall, C. Hall, J. C. Day, and N. Stone, "Evaluation of a multi-fibre needle raman probe for tissue analysis," Proc. SPIE **9704**, 97040G (2016).
14. J. Shubert and M. A. L. Bell, "Photoacoustic imaging of a human vertebra: implications for guiding spinal fusion surgeries," Phys. Med. Biol. **63**(14), 144001 (2018).
15. E. A. Gonzalez, A. Jain, and M. A. L. Bell, "Combined ultrasound and photoacoustic image guidance of spinal pedicle cannulation demonstrated with intact ex vivo specimens," IEEE Trans. Biomed. Eng. **68**(8), 2479–2489 (2021).
16. L. Liu, Y. Zhao, A. Li, X. Yu, X. Xiao, S. Liu, and M. Q.-H. Meng, "A photoacoustics-enhanced drilling probe for radiation-free pedicle screw implantation in spinal surgery," Front. Bioeng. Biotechnol. **10**, 1000950 (2022).
17. T. J. Farrell, M. S. Patterson, and B. Wilson, "A diffusion theory model of spatially resolved, steady-state diffuse reflectance for the noninvasive determination of tissue optical properties in vivo," Med. Phys. **19**(4), 879–888 (1992).
18. D. Evers, B. Hendriks, G. Lucassen, and T. Ruers, "Optical spectroscopy: current advances and future applications in cancer diagnostics and therapy," Future Oncol. **8**(3), 307–320 (2012).
19. R. Doornbos, R. Lang, M. Aalders, F. Cross, and H. Sterenborg, "The determination of in vivo human tissue optical properties and absolute chromophore concentrations using spatially resolved steady-state diffuse reflectance spectroscopy," Phys. Med. Biol. **44**(4), 967–981 (1999).
20. M. Duperron, K. Grygoryev, G. Nunan, C. Eason, J. Gunther, R. Burke, K. Manley, and P. O'brien, "Diffuse reflectance spectroscopy-enhanced drill for bone boundary detection," Biomed. Opt. Express **10**(2), 961–977 (2019).
21. C. Fisher, J. Harty, A. Yee, C. L. Li, K. Komolibus, K. Grygoryev, H. Lu, R. Burke, B. C. Wilson, and S. Andersson-Engels, "Perspective on the integration of optical sensing into orthopedic surgical devices," J. Biomed. Opt. **27**(01), 010601 (2022).
22. M. S. Losch, A. Swamy, A. Elmi-Terander, E. Edström, B. H. Hendriks, and J. Dankelman, "Proton density fat fraction of the spinal column: an mri cadaver study," Biomed. Eng. Online **20**(1), 7–11 (2021).
23. R. Van Veen, H. J. Sterenborg, A. Pifferi, A. Torricelli, E. Chikoidze, and R. Cubeddu, "Determination of visible near-ir absorption coefficients of mammalian fat using time-and spatially resolved diffuse reflectance and transmission spectroscopy," J. Biomed. Opt. **10**(5), 054004 (2005).
24. A. Swamy, G. Burström, J. W. Spliethoff, D. Babic, C. Reich, J. Groen, E. Edström, A. E. Terander, J. M. Racadio, J. Dankelman, and B. H. Hendriks, "Diffuse reflectance spectroscopy, a potential optical sensing technology for the detection of cortical breaches during spinal screw placement," J. Biomed. Opt. **24**(01), 1 (2019).
25. G. Burström, A. Swamy, J. W. Spliethoff, C. Reich, D. Babic, B. H. Hendriks, H. Skulason, O. Persson, A. E. Terander, and E. Edström, "Diffuse reflectance spectroscopy accurately identifies the pre-cortical zone to avoid impending pedicle screw breach in spinal fixation surgery," Biomed. Opt. Express **10**(11), 5905–5920 (2019).
26. A. M. J. Wang, J. E. Bender, J. Pfefer, U. Utzinger, and R. A. Drezek, "Depth-sensitive reflectance measurements using obliquely oriented fiber probes," J. Biomed. Opt. **10**(4), 044017 (2005).
27. R. E. Thilwind, G. W. t'Hooft, and N. Uzunbajakava, "Improved depth resolution in near-infrared diffuse reflectance spectroscopy using obliquely oriented fibers," J. Biomed. Opt. **14**(2), 024026 (2009).
28. K. J. Chung, S. W. Suh, S. Desai, and H. R. Song, "Ideal entry point for the thoracic pedicle screw during the free hand technique," Int. Orthop. **32**(5), 657–662 (2008).
29. D. Marti, R. Aasbjerg, P. E. Andersen, and A. K. Hansen, "Mcmatlab: an open-source user-friendly matlab-integrated 3d monte carlo light transport solver with heat diffusion and tissue damage," J. Biomed. Opt. **23**(12), 1 (2018).
30. S. Jacques, T. Li, and S. Prahl, "MCXYZ," OMLC, 2019, https://omlc.org/software/mc/mcxyz/index.html.
31. R. Nachabe, B. H. Hendriks, A. E. Desjardins, M. Van Der Voort, M. B. Van Der Mark, and H. J. Sterenborg, "Estimation of lipid and water concentrations in scattering media with diffuse optical spectroscopy from 900 to 1600 nm," J. Biomed. Opt. **15**(3), 037015 (2010).
32. I. Driver, J. Feather, P. King, and J. Dawson, "The optical properties of aqueous suspensions of intralipid, a fat emulsion," Phys. Med. Biol. **34**(12), 1927–1930 (1989).
33. S. T. Flock, S. L. Jacques, B. C. Wilson, W. M. Star, and M. J. van Gemert, "Optical properties of intralipid: a phantom medium for light propagation studies," Lasers Surg. Med. **12**(5), 510–519 (1992).
34. B. W. Pogue and M. S. Patterson, "Review of tissue simulating phantoms for optical spectroscopy, imaging and dosimetry," J. Biomed. Opt. **11**(4), 041102 (2006).

Biomedical Optics EXPRESS

35. S. A. Amiri, P. Van Berckel, M. Lai, J. Dankelman, and B. H. Hendriks, "Tissue-mimicking phantom materials with tunable optical properties suitable for assessment of diffuse reflectance spectroscopy during electrosurgery," Biomed. Opt. Express **13**(5), 2616–2643 (2022).
36. V. V. Tuchin, "Tissue optics and photonics: light-tissue interaction," J. Biomed. Photonics Eng. **1**, 98–134 (2015).
37. L. G. Henyey and J. L. Greenstein, "Diffuse radiation in the galaxy," Astrophys. J. **93**, 70–83 (1941).
38. T. Vo-Dinh, *Biomedical Photonics Handbook* (CRC press, 2003).
39. V. V. Tuchin, "Tissue optics and photonics: biological tissue structures," J. Biomed. Photonics Eng. **1**(1), 3–21 (2015).
40. D. F. Swinehart, "The beer-lambert law," J. Chem. Educ. **39**(7), 333 (1962).
41. F. Fanjul-Vélez, S. Pampín-Suárez, and J. L. Arce-Diego, "Application of classification algorithms to diffuse reflectance spectroscopy measurements for ex vivo characterization of biological tissues," Entropy **22**(7), 736 (2020).
42. S. Ruschke, A. Pokorney, T. Baum, H. Eggers, J. H. Miller, H. H. Hu, and D. C. Karampinos, "Measurement of vertebral bone marrow proton density fat fraction in children using quantitative water–fat mri," MAGMA **30**(5), 449–460 (2017).
43. D. J. Evers, R. Nachabe, M.-J. Vranken Peeters, J. A. van der Hage, H. S. Oldenburg, E. J. Rutgers, G. W. Lucassen, B. H. Hendriks, J. Wesseling, and T. J. Ruers, "Diffuse reflectance spectroscopy: towards clinical application in breast cancer," Breast Cancer Res. Treat. **137**(1), 155–165 (2013).
44. L. De Boer, B. Molenkamp, T. Bydlon, B. Hendriks, J. Wesseling, H. Sterenborg, and T. Ruers, "Fat/water ratios measured with diffuse reflectance spectroscopy to detect breast tumor boundaries," Breast Cancer Res. Treat. **152**(3), 509–518 (2015).
45. D. Evers, R. Nachabe, D. Hompes, F. Van Coevorden, G. Lucassen, B. Hendriks, M.-L. van Velthuysen, J. Wesseling, and T. Ruers, "Optical sensing for tumor detection in the liver," Eur. J. Surg. Oncol. **39**(1), 68–75 (2013).
46. J. P. Rathmell, A. E. Desjardins, M. van der Voort, B. H. Hendriks, R. Nachabe, S. Roggeveen, D. Babic, M. Söderman, M. Brynolf, and B. Holmström, "Identification of the epidural space with optical spectroscopy: an in vivo swine study," Anesthesiology **113**(6), 1406–1418 (2010).
47. A. Balthasar, A. E. Desjardins, M. van der Voort, G. W. Lucassen, S. Roggeveen, K. Wang, W. Bierhoff, A. G. Kessels, M. van Kleef, and M. Sommer, "Optical detection of peripheral nerves: an in vivo human study," Reg. Anesth. Pain Med. **37**(3), 277–282 (2012).
48. M. S. Losch, F. Kardux, J. Dankelman, and B. H. Hendriks, "Steering light in fiber-optic medical devices: a patent review," Expert Rev. Med. Devices **19**(3), 259–271 (2022).
49. R. Gunaratne, J. Goncalves, I. Monteath, R. Sheh, M. Kapfer, R. Chipper, B. Robertson, R. Khan, D. Fick, and C. N. Ironside, "Wavelength weightings in machine learning for ovine joint tissue differentiation using diffuse reflectance spectroscopy (DRS)," Biomed. Opt. Express **11**(9), 5122–5131 (2020).
50. M. S. Losch, "Data underlying the publication: "Diffuse reflectance spectroscopy of the spine: Improved breach detection with angulated fibers"," Delft University of Technology, 2022, https://doi.org/10.4121/20332305.